Journal of Electroceramics, 7, 57–66, 2001

Synthesis, Physicochemical Characterization and Ionic Conductivity of $LaGa_{0.4}Mg_{0.2}M_{0.4}O_{3-\delta}$ (M = Cr, Mn, Fe, Co)

V.V. KHARTON,[1,2] A.A. YAREMCHENKO,[2] A.P. VISKUP,[2] G.C. MATHER,[1] E.N. NAUMOVICH[2] & F.M.B. MARQUES[1]

[1]*Department of Ceramics and Glass Engineering, UIMC, University of Aveiro, 3810-193 Aveiro, Portugal*
[2]*Institute of Physicochemical Problems, Belarus State University, 14 Leningradskaya Str., 220080 Minsk, Republic of Belarus*

Submitted October 18, 2000; Revised February 26, 2001; Accepted March 7, 2001

Abstract. Partial electronic and ionic conductivities, crystal structure, thermal expansion and infrared absorption spectra of the perovskite-type series, $LaGa_{0.40}Mg_{0.20}M_{0.40}O_{3-\delta}$ (M = Cr, Mn, Fe and Co), have been studied. The rhombohedral distortion of the perovskite lattice decreases and the unit cell volume increases in the sequence Co < Cr < Mn < Fe. The *p*-type electronic conduction increases with atomic number of the transition metal cation; the activation energy varies in air from 15.9 to 32.1 kJ/mol. The oxygen ionic conductivity of the M-doped phases at temperatures below 1200 K is significantly lower than that of $LaGa(Mg)O_3$. The highest ionic conductivity was found for the Fe- and Co-containing phases. The ion transference numbers of $La(Ga,Mg,M)O_{3-\delta}$ at 970–1270 K were determined to vary in a wide range, from 2×10^{-5} to 3×10^{-2}. Thermal expansion coefficients, calculated from the dilatometric data collected in the temperature range 300–1100 K, lie in the range $(7.2–15.5) \times 10^{-6}$ K^{-1}.

Keywords: perovskite, lanthanum gallate, transference number, thermal expansion, mixed conductor

1. Introduction

The impetus to find materials with greater oxygen-ion conductivity than the current solid oxide fuel cell (SOFC) electrolyte of choice, yttria-stabilized zirconia, has resulted in much recent research devoted to a class of perovskite phases based on lanthanum gallate, $LaGaO_3$ [1–9]. These phases are of interest, not only for intermediate temperature electrolyte applications, but also as mixed ionic-electronic conductors for use as oxygen-separation membranes and electrochemical reactors for the partial oxidation of hydrocarbons [5, 6]. High ionic conduction is achieved by doping the perovskite (ABO_3) with lower valence cations on the A and/or B sites, including the substitution of La with alkaline-earth cations (Sr, Ca, Ba) and Ga with bivalent metal cations (Mg, Ni). One of the highest oxygen-ion conductivities of any material occurs for the solid solution series $(La,Sr)(Ga,Mg)O_{3-\delta}$ (LSGM). The stability of the perovskite lattice permits a wide variety of substitutions with the effect that the electrochemical and chemical properties can be tailored to a considerable degree. For example, high levels of mixed conductivity have been found in a large number of systems by doping the base $LaGaO_3$ material with a host of transition metal cations [5–11].

The present work continues our research [6, 9–15] focusing on the transport and physicochemical properties of $LaGa(Mg)O_{3-\delta}$ doped with large concentrations of transition metals. This study is of importance to the understanding of ionic and electronic transport mechanisms in lanthanum gallates in the search for improved mixed conductor materials and in determining the properties of likely reaction products between doped $LaGaO_3$ and oxide components of electrochemical cells, e.g. $LaMO_3$, M = Cr, Mn, Fe, Co [16, 17]. In addition, the substitution of expensive Ga with other cations may lower production costs and suppress some of the other disadvantages of $LaGaO_3$-based materials, including volatilization of Ga_2O during high temperature sintering and reduction of Ga (III) cations at anode-electrolyte interfaces [18–20]. In this work, particular

attention has been paid to the effect of preparation route on phase composition, structure and transport properties of La(Ga,Mg,M)$O_{3-\delta}$ solid solutions.

2. Experimental

Solid-state synthesis of $LaGa_{0.40}Mg_{0.20}M_{0.40}O_{3-\delta}$ (M = Cr, Mn, Fe, Co) and $LaGa_{1-x}Mg_xO_{3-\delta}$ (x = 0.15 and 0.20) was performed using a standard ceramic processing route. The compositions studied are designated by abbreviations, listed in Table 1. Two preparation techniques were employed for synthesis of $LaGa_{0.40}Mg_{0.20}M_{0.40}O_{3-\delta}$. The first, referred to hereafter as Method I, involved dissolving stoichiometric amounts of metal oxides, nitrates or acetates in an aqueous solution of nitric acid with additions of hydrogen peroxide, with subsequent drying and thermal decomposition of the nitrate mixtures. The purity of the starting materials was no less than 99.95% in the case of oxides and 99.5% for the metal salts. In the second synthesis route, Method II, stoichiometric mixtures of the binary-metal oxides were firstly prereacted at 1370 K and then ball-milled. Both preparation routes involved annealing of the resultant oxide mixtures in a temperature range of 1520–1670 K for 30–40 h with multiple intermediate regrindings; the powders were then pressed (350–500 MPa) into bars ($4 \times 4 \times 30$ mm) and disks of various thicknesses (diameter of 12 and 15 mm) before firing in air at 1800–1870 K for 6–10 hours. The preparation procedure for La(Ga,Mg)$O_{3-\delta}$ involved synthesis by Method I and an alternative synthesis technique employing the binary oxide mixtures which were pre-reacted at 1370 K, then pressed and sintered at 1870 K [15].

Physicochemical and structural characterization of the reaction products was carried out by X-ray diffraction (XRD), scanning electron microscopy (SEM), emission spectroscopic analysis, infrared (IR) absorption spectroscopy, thermal gravimetric and differential thermal analysis (TGA/DTA), and dilatometry. Transport properties were studied using impedance spectroscopy (IS), 4-probe DC conductivity measurements, Faradaic efficiency measurements (FE), steady-state oxygen permeability (OP) and the e.m.f. of oxygen concentration cells (EMF). Details of experimental procedures and equipment can be found in [6, 9–15] and references therein.

Table 1. List of abbreviations.

Composition	Abbreviation
$LaGa_{0.40}Mg_{0.20}Cr_{0.40}O_{3-\delta}$	LGM20Cr40
$LaGa_{0.40}Mg_{0.20}Mn_{0.40}O_{3-\delta}$	LGM20Mn40
$LaGa_{0.40}Mg_{0.20}Fe_{0.40}O_{3-\delta}$	LGM20Fe40
$LaGa_{0.40}Mg_{0.20}Co_{0.40}O_{3-\delta}$	LGM20Co40
$LaGa_{0.85}Mg_{0.15}O_{3-\delta}$	LGM15
$LaGa_{0.80}Mg_{0.20}O_{3-\delta}$	LGM20

The oxygen ionic transference numbers of samples measured by these different techniques (OP, FE, EMF) are, within the limits of experimental error, similar; comparative results of these experiments have been published elsewhere [12, 14, 21]. In the case of oxygen permeation measurements, the transference number (t_o) was calculated according to the equation:

$$t_o(1 - t_o) \cdot \sigma = \frac{16F^2 d}{RT} \cdot \left. \frac{\partial j}{\partial \ln(p_2/p_1)} \right|_{p_1 \to p_2} \quad (1)$$

where σ is the total conductivity, d is the membrane thickness, j is the permeation flux density, and p_1 and p_2 are the oxygen partial pressures at the membrane permeate side and feed side, respectively. For all the data presented here, the value of p_2 was kept constant (21 kPa). Equation (1) is only valid in the case where the surface exchange kinetics is fast enough to have negligible influence on the permeation flux. The dependence of the flux on the membrane thickness was, therefore, checked in order to determine the effect of the surface exchange rate on oxygen permeability. It can be seen in Fig. 1 that the oxygen permeability, $J(O_2)$, is essentially independent of membrane thickness at $d \geq 0.5$ mm within the experimental error limits. Values of $J(O_2)$ were calculated as [10, 11]:

$$J(O_2) = jd \cdot \left[\ln\left(\frac{p_2}{p_1}\right) \right]^{-1} \quad (2)$$

Since $J(O_2)$ is proportional to $j \times d$ by definition, the permeation fluxes are limited predominantly by the bulk ambipolar conductivity and not the surface exchange rate; Eq. (1) is, thus, valid in this instance. Faradaic efficiency measurements were performed under negligible oxygen chemical potential gradient in atmospheric air, as described in Ref. [14].

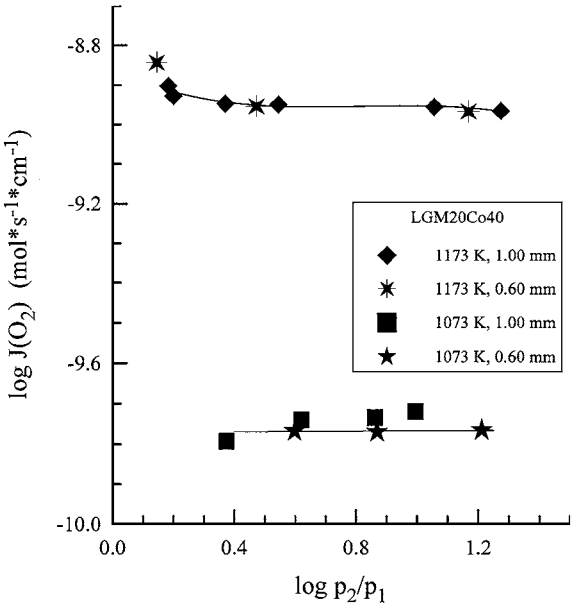

Fig. 1. Dependence of specific oxygen permeability of LGM20Co40 membranes on oxygen partial pressure difference. Solid lines are for visual guidance only.

3. Results and Discussion

3.1. Phase Composition

The XRD powder patterns of the prepared materials indicated the formation of perovskite-type phase. Phase purity for the samples prepared by Method I was significantly better than that of the Method II compositions. However, a few unidentified reflections whose intensity did not exceed 3–4% of the most intense perovskite reflection were found in the XRD patterns of the Method I compositions (Fig. 2). The minor unidentified peaks found in all the $LaGa_{0.40}Mg_{0.20}M_{0.40}O_{3-\delta}$ (M = Cr, Mn, Fe) samples were found at 2θ angles of 25.5–25.6° and 38.2–38.3° (Cu K_α-radiation); very small reflections at 47.9–48.3° and 53.7–54.1° were also observed in the case of LGM20Cr40 and LGM20Fe40 prepared by Method I. In contrast, the Method II preparation procedure resulted in significantly greater amounts of La_2O_3 and $La_4Ga_2O_9$ for all compositions. Figure 3 shows the XRD pattern of $LaGa_{0.40}Mg_{0.20}Cr_{0.40}O_{3-\delta}$ prepared by Method II. LGM15 was single-phase when synthesised from metal-salt precursors but contained MgO impurity when prepared from the binary oxides, as reported in detail elsewhere [15]. All attempts to synthesize

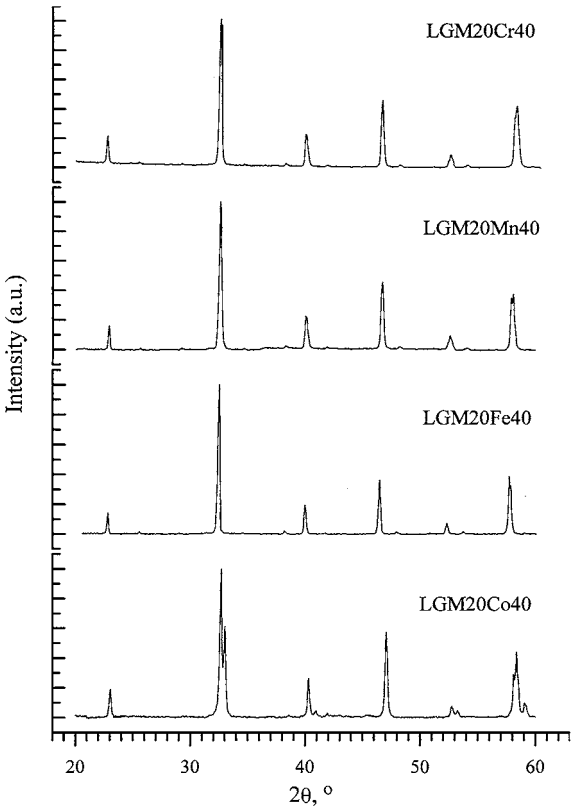

Fig. 2. Powder XRD patterns of the $La(Ga,Mg,M)O_{3-\delta}$ phases prepared by Method I.

phase-pure LGM20 were unsuccessful, with significant amounts of MgO and $MgGa_2O_4$ being present; this composition was not, therefore, subjected to detailed study.

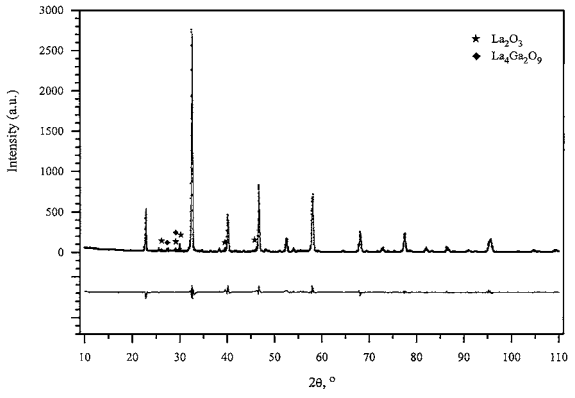

Fig. 3. The observed, calculated and difference powder XRD profiles for LGM20Cr40 prepared by Method II. The marked reflections of the impurity phases were excluded for the structure refinement.

Table 2. Properties of La(Ga,Mg,M)$O_{3-\delta}$ phases prepared by Method I.

		Unit cell parameters		Average thermal expansion coefficients	
Abbreviation	Structure	a (nm)	α,°	T (K)	$\overline{\alpha} \times 10^6$, K^{-1}
LGM20Cr40	R[a]	0.5503	60.22	300–670	7.2 ± 0.2
				670–1060	10.65 ± 0.05
LGM20Mn40	R	0.5512	60.20	300–540	7.8 ± 0.3
				610–1100	10.2 ± 0.1
LGM20Fe40	R	0.5530	60.12	300–870	9.0 ± 0.1
				870–1080	14.1 ± 0.4
LGM20Co40	R	0.5437	60.68	300–1100	15.5 ± 0.3
LGM15	R	0.5526	60.17	300–1100	10.1 ± 0.1

[a]"R" corresponds to the rhombohedrally distorted perovskite structure.

Synthesis from binary metal oxides appears to be inappropriate for obtaining phase-pure heavily doped $LaGaO_3$-based phases. The formation of secondary phases is most probably caused by volatilization of Ga_2O in the course of firing. The liquid-phase reactants are more reactive so it is possible that formation of perovskite at particle surfaces during solid-state synthesis suppresses further volatilization of gallium oxide whereas the reaction rate in the mixture obtained from binary oxides is expected to be lower, which may lead to larger losses of gallium. However, neither decreasing the reaction temperature nor synthesis time resulted in single-phase perovskite in this case.

3.2. *Crystal Structure*

Further inspection of the powder patterns of the Method I compositions indicated that the main perovskite-type phase is rhombohedrally distorted; the unit cell parameters (**a** and α) are given in Table 2. The **a** parameter and unit cell volume both increase in the sequence M = Co < Cr < Mn < Fe with corresponding increase in the B-site cation radius (the radii of the trivalent transition metal cations with high-spin configuration decrease in the order Fe = Mn > Cr > Co [22]). Since Mn has a higher average oxidation state in the B-site of the perovskite structure [23] and, therefore, smaller cation radius than iron [22], the smaller unit cell volume of LGM20Mn40 in comparison with LGM20Fe40 may be attributed to the change in the dopant cation size. Distortion of the perovskite lattice, expressed by the rhombohedral angle α, exhibit opposite behavior, decreasing in the order Co > Cr > Mn > Fe (Table 2).

For compositions synthesized by Method II, the unit cell volume also increases in the sequence Cr < Mn < Fe (Table 3). In this case, however, the structure was identified as an orthorhombic $GdFeO_3$-type perovskite. The difference in symmetries among compositions synthesised by different techniques is most probably associated with the degree of volatilization of gallium oxide and subsequent segregation of secondary phases. It is known that the lattice symmetry of lanthanum gallates depends strongly on cation composition. For example, a transition from orthorhombic to rhombohedral symmetry was found by high-resolution neutron diffraction for both $LaGaO_3$ and $La_{0.9}Sr_{0.1}Ga_{0.8}Mg_{0.2}O_{2.85}$ at temperatures as low as about 523 K [24]. The rhombohedral distortion in the Sr- and Mg-doped sample was smaller than that of the undoped lanthanum gallate [24]. It is clear, therefore, that small variations in the composition may result in changes in lattice symmetry.

Structural refinement of the LGM20Cr40 orthorhombic phase (Fig. 2, Table 4) was carried out by the Rietveld method using the structural parameters of $LaGaO_3$ (S.G.: Pnma) as a starting model. The

Table 3. XRD data on La(Ga,Mg,M)$O_{3-\delta}$ phases prepared by Method II.

		Unit cell parameters		
Abbreviation	Structure	a (nm)	b (nm)	c (nm)
LGM20Cr40	O[a]	0.5497	0.7781	0.5526
LGM20Mn40	O	0.5505	0.7795	0.5535
LGM20Fe40	O	0.5523	0.7815	0.5544
LGM15	O	0.5518	0.7839	0.5549

[a]"O" corresponds to the orthorhombically distorted perovskite structure.

Table 4. Structure refinement data for $LaGa_{0.40}Mg_{0.20}Cr_{0.40}O_{3-\delta}$ prepared by Method II.

Atom	Position	x/*a*	y/*b*	*c*/z	B (Å^3)	Site
La	*4c*	0.0185(2)	0.25	−0.0033(5)	1.08(3)	1.0(−)
Ga/Cr/Mg	*4b*	0	0	0.5	0.67(4)	0.4/0.4/0.2(−)
O(1)	*4c*	−0.005(1)	0.25	0.439(3)	0.4(1)	0.967(−)
O(2)	*8d*	0.256(7)	0.460(2)	−0.267(3)	0.4(1)	1.933(−)

Selected bond lengths (in Å)		Selected angles	
La—O(2)	3.12(2) × 2	O(1)—Ga/Cr/Mg—O(1)	180
La—O(2)	2.85(1) × 2	O(1)—Ga/Cr/Mg—O(2)	92.3(6) × 2
La—O(2)	2.59(1) × 2	O(1)—Ga/Cr/Mg—O(2)	91.1(6) × 2
La—O(2)	2.49(1) × 2	O(1)—Ga/Cr/Mg—O(2)	88.9(6) × 2
La—O(1)	3.08(2)	O(1)—Ga/Cr/Mg—O(2)	87.7(6) × 2
La—O(1)	2.90(2)	O(2)—Ga/Cr/Mg—O(2)	180 × 2
La—O(1)	2.64(2)	O(2)—Ga/Cr/Mg—O(2)	92.1(6) × 2
La—O(1)	2.45(2)	O(2)—Ga/Cr/Mg—O(2)	87.9(6) × 2
Ga/Cr/Mg—O(2)	2.09(1) × 2		
Ga/Cr/Mg—O(2)	1.86(1) × 2		
Ga/Cr/Mg—O(1)	1.97(4) × 2		

S.G: Pnma; $a = 5.4968(2)$, $b = 7.7807(3)$, $c = 5.5265(2)$ Å; $R_I = 6.69\%$, $R_p = 9.66\%$, $R_{wp} = 14.1\%$, $R_{exp} = 17.35\%$.

background was interpolated linearly from a suitable number of points and the profile was described by a pseudo-Voigt profile-shape function and four asymmetry parameters to describe peaks below $2\theta = 40^\circ$. The range $25.8^\circ \leq 2\theta \leq 30.6^\circ$ containing the principal reflections of La_2O_3 and $La_4Ga_2O_9$ was omitted from the refinement. No reflections were present at 2θ angles low enough to indicate the formation of a perovskite supercell as a result of either B-cation or oxygen-vacancy order. The Ga, Cr and Mg cations were, thus, disordered over the B-cation site and given a common isothermal temperature factor (B). Refinement of the oxygen-site occupancies indicated that the oxygen-vacancy concentration was averaged over the O(1) and O(2) sites; the O occupancies were held invariant in the final refinement in order to avoid correlation with the oxygen thermal vibration factors.

The BO_6 octahedra in the Cr- and Mg-containing phase were found to be somewhat distorted in comparison to both $LaGaO_3$ and $La_{0.9}Sr_{0.1}Ga_{0.8}Mg_{0.2}O_{2.85}$ [25], with the B—O bond length ranging from 0.186 to 0.209 nm. The average B—O bond length, 0.197 nm, is, however, similar to that of the parent phase, LGM15 [15]. In a similar study of Nb-doped $LaGa(Mg)O_{3-\delta}$ compositions, the BO_6 octahedra were also very irregular in the Nb-containing phases, although, in this case, the degree of distortion was much greater [15]. The A-cation sites are also distorted in LGM20Cr40 (bond length ranges from 0.245 to 0.312 nm), the common orthorhombic distortion from the cubic isotype arising when the A-cation is too small for its cuboctahedral site.

3.3. Total Conductivity

Comparative analysis of the transport properties of the materials prepared by the different techniques indicated that the total electrical conductivity of samples with predominantly ionic conduction is significantly affected by the presence of impurity phases. Conversely, in the case of primarily electronic conductors, the influence of impurity phases on the conductivity is minimal (Fig. 4). For instance, segregation of MgO in LGM15 leads to both lower conductivity and activation energy at temperatures above 770 K; literature data [3, 4] also indicates an increase in the activation energy for ionic transport when the magnesium content is increased. In contrast, the total electrical conductivity of LGM20Cr40 with predominant electronic transport (Fig. 5) is essentially independent of preparation route (Fig. 4). A possible reason for this is

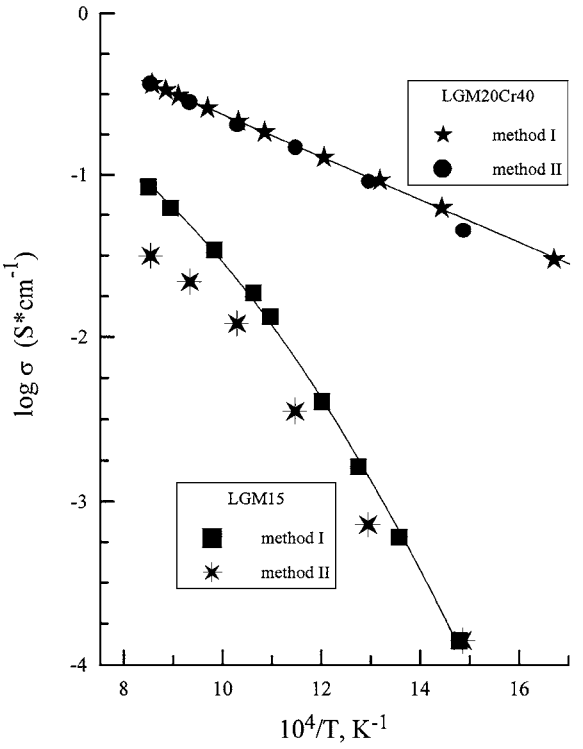

Fig. 4. Temperature dependence of the total conductivity in air of $LaGaO_3$-based ceramics prepared by different techniques.

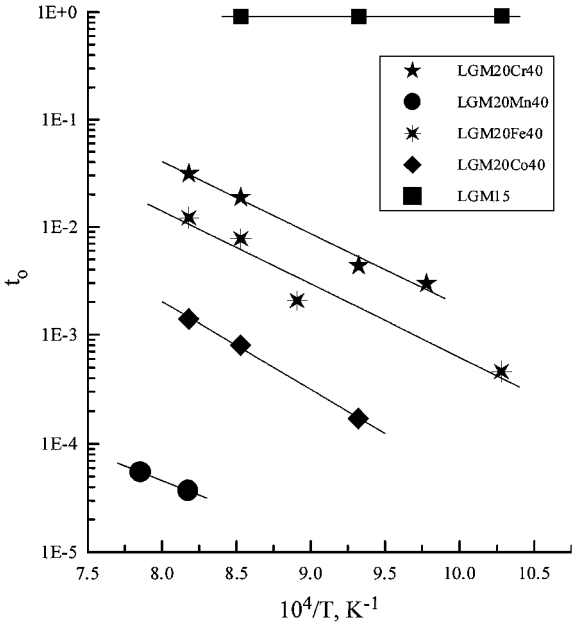

Fig. 5. Temperature dependence of the oxygen-ion transference numbers of $LaGaO_3$-based phases prepared by the Method I at oxygen partial pressures close to atmospheric air. The measurement techniquesemployed are the following: FE (LGM20Cr40, LGM20Mn40 and LGM20Fe40), OP (LGM20Co40), and EMF (LGM15).

that the amount of low-conductivity phase, La_2O_3 and $La_4Ga_2O_9$, is significantly smaller than the percolation limit for electronic transport and, hence, has a weak effect on the conductivity. Furthermore, the formation of these phases results in a greater Cr and Mg concentration in the major perovskite phase, which may promote higher electronic conduction (see, for example [26] and references therein).

On inspection of the electrical properties of the end-member $LaGaO_3$- and $LaMO_3$-based compounds, it is expected that the electronic conductivity of the title materials increases with increasing content and atomic number of the transition metal cation (Fig. 6). Whereas the ion transference number of LGM15 is close to unity, the t_o values of $LaGa_{0.40}Mg_{0.20}M_{0.40}O_{3-\delta}$ do not exceed 3×10^{-2} (Fig. 5). As the transition metal dopant concentration exceeds the percolation limit (30–35%), electronic conduction dominates and takes place within a continuous network of M─O─M bonds. The conductivity increases in the sequence Cr < Mn < Fe < Co (Fig. 6), and reflects a transition from electron transport via the *p*-type small polaron mechanism, as in

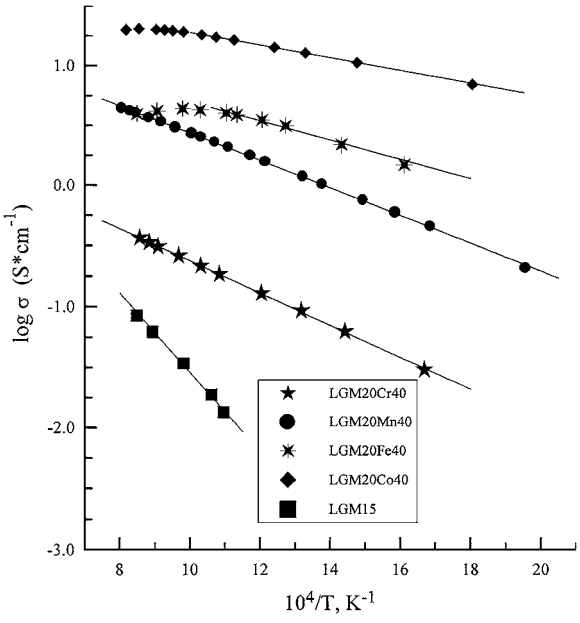

Fig. 6. Temperature dependence of the total conductivity in air of $LaGaO_3$-based ceramics prepared by Method I.

Table 5. Parameters of the Arrhenius model for the *p*-type electronic conductivity of $LaGaO_3$-based phases in air.

Abbreviation	T (K)	E_a (kJ/mol)	$\ln(A_0)$ (S/cm)
LGM20Cr40	560–1170	32.1 ± 0.3	9.34 ± 0.04
LGM20Mn40	300–1240	27.1 ± 0.3	11.15 ± 0.06
LGM20Fe40	300–980	25 ± 1	11.6 ± 0.2
LGM20Co40	430–1110	15.9 ± 0.2	11.73 ± 0.04
LGM15	873–1173	94 ± 8	12 ± 1

$LaCrO_{3-\delta}$, to pseudo-metallic behavior, characteristic of $LaCoO_{3-\delta}$ at high temperatures ([26, 27] and references therein). The effective activation energy, E_a, of the electronic conductivity, was calculated by the standard Arrhenius model:

$$\sigma = \frac{A_0}{T} \cdot \exp\left(-\frac{E_a}{RT}\right) \quad (3)$$

where A_0 is the pre-exponential factor. The activation energy decreases in the sequence Cr > Mn > Fe > Co (Table 5), indicating a progressive delocalization of the atomic orbitals and increasing bandwidth with increasing atomic number. Correspondingly, the conductivity of Fe- and Co-doped phases becomes metallic-like at temperatures above 1000–1100 K, whilst the temperature dependence of the conductivity of Cr- and Mn-containing perovskites is linear in Arrhenius coordinates throughout the studied temperature range (Fig. 6).

3.4. *Ionic Transport*

Ionic transport data for the $LaGa_{0.40}Mg_{0.20}M_{0.40}O_{3-\delta}$ series in air are presented in Fig. 7 and Table 6. The activation energy for oxygen ionic conductivity, calculated using Eq. (3), is similar for all compositions, varying

Table 6. Parameters of the Arrhenius model for the ionic conductivity of $LaGaO_3$-based phases in air.

Abbreviation	T (K)	E_a (kJ/mol)	$\ln(A_0)$ (S/cm)
LGM20Cr40	1023–1223	161 ± 10	19 ± 1
LGM20Mn40	1223–1273	134	11.6
LGM20Fe40	973–1223	135 ± 19	17 ± 2
LGM20Co40	1073–1223	163 ± 8	19.6 ± 0.9
LGM15	873–1173	72 ± 5	11.9 ± 0.6

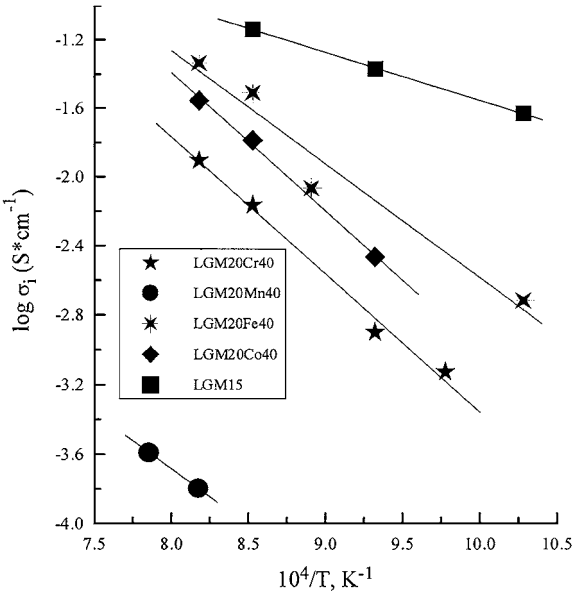

Fig. 7. Temperature dependence of the partial oxygen ionic conductivity in air of $LaGaO_3$-based ceramics prepared by the Method I.

in the range 134–163 kJ/mol. The ionic conductivity changes in the sequence Mn < Cr < Co ≤ Fe. The reason for the greater conductivity of Fe-doped gallate in comparison with its Co-containing analogue is most likely due to the smaller distortion of the crystal lattice of the former, resulting in a more degenerate system of conduction pathways. Further evidence of this is provided by the fact that compositions with a more distorted structure (LGM20Cr40 and LGM20Co40) exhibit a slightly higher activation energy for ionic conduction (161–163 kJ/mol).

The oxygen conductivity of LGM20Cr40 is lower than that for Fe- and Co-doped analogues due to the higher Cr—O bond strength; typically, the oxygen vacancy diffusion coefficients in doped $LaCrO_{3-\delta}$ are significantly smaller than in ferrites and cobaltites (for example, [28]). Another factor that may explain the lower conductivity of the Cr-doped phase, however, is its lower oxygen-vacancy concentration in comparison with the Fe- and Co-containing perovskites [23]. A less-well understood case is that of the Mn-doped gallate with ionic conductivity lower than LGM20Cr40 by about two orders of magnitude. Again, the poor conductivity is most probably associated with a lower oxygen-vacancy concentration and a higher strength of Mn—O bonds. For instance, preliminary TGA tests in hydrogen indicated that the oxygen

content in LGM20Mn40 is close to stoichiometric. A more precise determination of the oxygen nonstoichiometry of this material is now in progress; these tests are complicated, however, by the possible volatilization of Ga_2O in reducing conditions at temperatures above 1370 K (at lower temperatures the reduction of LGM20Mn40 is stagnated due to thermodynamic and kinetic reasons).

A detailed analysis of the ionic conductivity of the gallates heavily doped with transition metals has been conducted previously [12, 21] and is not included here. To summarise, the doped phases have significanlty lower ionic conduction than the base material. This may be due to ordering in the oxygen sublattice, resulting from either association of oxygen vacancies with bivalent cations (Mg^{2+}, M^{2+}) or formation of stable M^{4+}–O–Mg^{2+} pairs where the tetravalent cations are likely to inhibit anionic migration through Coulombic attraction.

3.5. Thermal Expansion and IR Absorption

Average thermal expansion coefficients (TECs) of the studied materials, calculated from dilatometric data collected in air, vary in the range (7.2–15.5) $\times$ $10^{-6}\,K^{-1}$ (Table 2). Some anomalous data with near zero expansion was observed in the dilatometric curves of $LaGa_{0.40}Mg_{0.20}M_{0.40}O_{3-\delta}$ (M = Cr, Mn and Fe) around 800 K within a narrow temperature range of 15–25 K. At higher and lower temperatures, however, the thermal expansion exhibited the expected linear behaviour. This anomolous event has been observed previously for several $LaGaO_3$-based phases [29], where it was discussed in terms of phase transitions.

The average TEC values of the $La(Ga,Mg,M)O_{3-\delta}$ solid solutions were found to increase with increasing atomic number of the transition metal. This may be associated with increasing oxygen nonstoichiometry [23, 29]. One can also observe a correlation between TEC and ionic conductivity (Table 2 and Fig. 7); according to the phenomenological theory of ionic transport in solids [30], higher ionic conductivity may be ascribed to a lower energetic potential barrier for ion hopping when the crystal lattice expands.

The IR absorption spectra of the $La(Ga,Mg,M)O_{3-\delta}$ family of phases (Fig. 8) are typical of perovskite-type oxides [31, 32], and consist of stretching and bending vibration bands at 580–650 and 360–460 cm^{-1}, respectively. The marked peaks (Fig. 8) were collected with a threshold condition of 0.5% of the transmittance (the height of selected peaks, defined as the smallest difference in height between a peak and the base on either side, was set at no less than 0.5% of the transmittance). The only exception to this condition is for the peaks at approximate positions of 588 and 640 cm^{-1} marked in the LGM20Cr40 spectrum; these peaks are formed due to splitting of the stretching vibration band. Due to peak overlap, a precise determination of their wavenumber is difficult. The IR absorption spectra of $La(Ga,Mg,M)O_{3-\delta}$ correspond to changes in crystal structure, as discussed above. In particular, there is a strong correlation between the stretching mode and unit cell volume (Fig. 8, Table 2). Phases with a large lattice distortion, for example Cr- and Co-doped perovskites, show splitting of the stretching vibration band as a result of differences in B—O bond length.

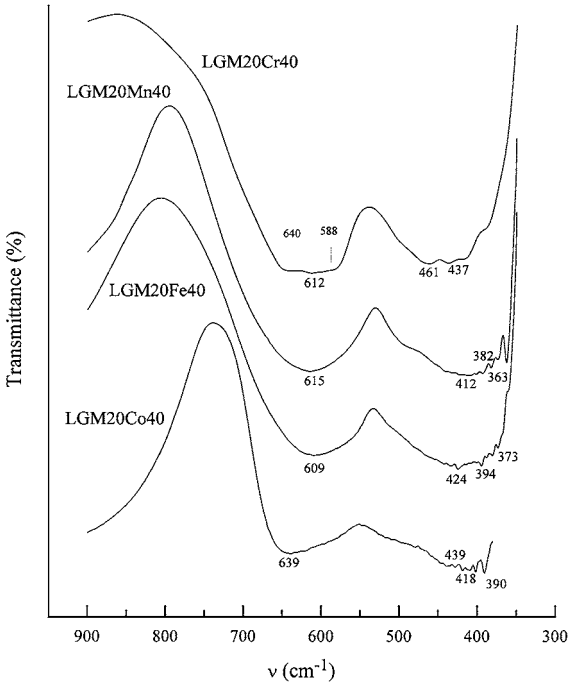

Fig. 8. IR absorption spectra at room temperature of La(Ga, Mg,M)$O_{3-\delta}$ phases prepared by Method I.

In summary, doping lanthanum gallate with high concentrations of transition metal cations increases the electronic conductivity to a considerable extent, but lowers ionic transport. In order, therefore, to optimize the performance of electrochemical cells employing

$LaGaO_3$-based solid electrolytes and $LaMO_3$ electrodes, considerable attention should be paid to ensuring that interdiffusion of the two materials is suppressed as much as possible. Similarly, to enhance the performance of doped gallate-based phases both as oxygen-separation membranes and electrolytes, a high concentration of bivalent dopant should be present in order to increase the ionic conductivity by increasing the oxygen-vacancy concentration and lowering the average positive charge in the cation sublattice.

4. Conclusions

The perovskite-type family of phases, $LaGa_{0.40}Mg_{0.20}M_{0.40}O_{3-\delta}$ (M = Cr, Mn, Fe and Co), were prepared by a standard ceramic synthesis technique. The crystal structure, IR absorption spectra, thermal expansion, and partial electronic and oxygen ionic conductivities have been studied. Synthesis from binary metal oxide precursors was found to result in the formation of secondary phases, most probably due to volatilization of gallium oxide. Preparation via a liquid phase, such as dissolution of precursors in nitric acid with subsequent thermal decomposition of the nitrate mixture, is a more successful route to obtaining phase-pure product. The distortion of the perovskite lattice decreases and the unit-cell volume increases in the sequence Co < Cr < Mn < Fe. Thermal expansion coefficients of the $La(Ga,Mg,M)O_{3-\delta}$ series over the temperature range 300–1100 K, are in the range $(7.2-15.5)\times10^{-6}\,K^{-1}$. *p*-type electronic conduction increases with atomic number of the transition metal cation; the activation energies for electronic conductivity in air vary from 15.9 to 32.1 kJ/mol. The ionic conductivity for all title materials at temperatures below 1200 K is significantly lower than that of Mg-doped $LaGaO_3$. The maximum oxygen ionic transport occurs for the Fe- and Co-doped phases, whereas the ionic conductivity of the Mn-containing phase in air was found to be extremely low. The values of the activation energy for oxygen ionic conductivity of the $La(Ga,Mg,M)O_{3-\delta}$ series lie in the range 134–163 kJ/mol.

Acknowledgments

This research was partially supported by the FCT (Praxis, Portugal), the Belarus Foundation for Basic Research and the Belarus State University.

References

1. T. Ishihara, H. Matsuda, and Y. Takita, *J. Am. Chem. Soc.*, **116**, 3801 (1994).
2. M. Feng and J.B. Goodenough, *Eur. J. Solid State Inorg. Chem.*, **31**, 663 (1994).
3. P. Huang and A. Petric, *J. Electrochem. Soc.*, **143**, 1644 (1996).
4. K. Huang, R.S. Tichy, and J.B. Goodenough, *J. Am. Ceram. Soc.*, **81**, 2565 (1998).
5. M. Schwartz, J.H. White, and A.F. Sammells, Int. Patent Application PCT WO 97/41060, 6 Nov. 1997.
6. V.V. Kharton, A.A. Yaremchenko, A.V. Kovalevsky, A.P. Viskup, E.N. Naumovich, and P.F. Kerko, *J. Membrane Sci.*, **163**, 307 (1999).
7. N. Trofimenko and H. Ullmann, *Solid State Ionics*, **118**, 215 (1999).
8. P. Huang, A. Horky, and A. Petric, *J. Am. Ceram. Soc.*, **82**, 2402 (1999).
9. R.T. Baker, B. Gharbage, and F.M.B. Marques, *J. Electrochem. Soc.*, **144**, 3130 (1997).
10. A.A. Yaremchenko, V.V. Kharton, A.P. Viskup, E.N. Naumovich, N.M. Lapchuk, and V.N. Tikhonovich, *J. Solid State Chem.*, **142**, 325 (1999).
11. A.A. Yaremchenko, V.V. Kharton, A.P. Viskup, E.N. Naumovich, V.N. Tikhonovich, and N.M. Lapchuk, *Solid State Ionics*, **120**, 65 (1999).
12. V.V. Kharton, E.N. Naumovich, and F.M.B. Marques, *Ionics*, **5**, 183 (1999).
13. R.T. Baker, B. Gharbage, and F.M.B. Marques, *J. Europ. Ceram. Soc.*, **18**, 105 (1998).
14. V.V. Kharton, A.A. Yaremchenko, A.P. Viskup, G.C. Mather, E.N. Naumovich, and F.M.B. Marques, *Solid State Ionics*, **128**, 79 (2000).
15. V.V. Kharton, A.P. Viskup, G.C. Mather, A.A. Yaremchenko, E.N. Naumovich, and F.M.B. Marques, *Bol. Soc. Esp. Ceram. Vidrio*, **38**, 647 (1999).
16. T. Ishihara, M. Honda, T. Shibayama, H. Minami, H. Nishiguchi, and Y. Takita, *J. Electrochem. Soc.*, **145**, 3177 (1998).
17. K. Huang, M. Feng, J.B. Goodenough, and C. Milliken, *J. Electrochem. Soc.*, **144**, 3620 (1997).
18. K. Yamaji, T. Horita, M. Ishikawa, N. Sakai, and H. Yokokawa, *Solid State Ionics*, **121**, 217 (1999).
19. J.W. Stevenson, T.R. Armstrong, L.R. Pederson, J. Li, C.A. Lewinsohn, and S. Baskaran, *Solid State Ionics*, **113**, 571 (1998).
20. E. Djurado and M. Labeau, *J. Europ. Ceram. Soc.*, **18**, 1397 (1998).
21. V.V. Kharton, A.P. Viskup, A.A. Yaremchenko, R.T. Baker, B. Gharbage, G.C. Mather, F.M. Figueiredo, E.N. Naumovich, and F.M.B. Marques, *Solid State Ionics*, **132**, 119 (2000).
22. R.D. Shannon, *Acta Cryst.*, **A32**, 751 (1976).
23. H.U. Anderson, *Solid State Ionics*, **52**, 33 (1992).
24. P.R. Slater, J.T.S. Irvine, T. Ishihara, and Y. Takita, in *Extend. Abstr. 11th Int. Conf. on Solid State Ionics* (International Society for Solid-State Ionics, Honolulu, 1997), p. 361.
25. P.R. Slater, J.T.S. Irvine, T. Ishihara, and Y. Takita, *Solid State Ionics*, **107**, 319 (1998).
26. V.V. Kharton, A.A. Yaremchenko, and E.N. Naumovich, *J. Solid State Electrochem.*, **3**, 303 (1999).

27. M.A. Senaris-Rodriguez, and J.B. Goodenough, *J. Solid State Chem.*, **116**, 224 (1995).
28. B.A. van Hassel, T. Kawada, N. Sakai, H. Yokokawa, M. Dokiya, and H.J.M. Bouwmeester, *Solid State Ionics*, **66**, 295 (1993).
29. H. Hayashi, M. Suzuki, and H. Inaba, *Solid State Ionics*, **128**, 131 (2000).
30. V.N. Chebotin, *Physical Chemistry of Solids* (Khimiya, Moscow, 1982) [in Russian].
31. Y.Y. Kim, D.H. Lee, T.Y. Kwon, and S.H. Park, *J. Solid State Chem.*, **112**, 376 (1994).
32. A. Arulraj and C.N.R. Rao, *J. Solid State Chem.*, **145**, 557 (1999).